# Enabling affordable omnidirectional subsurface extended image volumes via probing

**Tristan van Leeuwen[1], Rajiv Kumar[2] and Felix J. Herrmann[2]**

[1] *Mathematical Institute, Utrecht University, The Netherlands,*

[2] *Dept. of Earth Ocean and Atmospheric Sciences, University of British Columbia, Vancouver, BC, Canada*

*Email : T.vanLeeuwen@uu.nl, rajmittal09@gmail.com, fherrmann@eos.ubc.ca*

(November 30, 2015)

Running head: **Efficient extended imaging**

## ABSTRACT

Image gathers as a function of subsurface offset are an important tool for the inference of rock properties and velocity analysis in areas of complex geology. Traditionally, these gathers are thought of as multidimensional correlations of the source and receiver wavefields. The bottleneck in computing these gathers lies in the fact that one needs to store, compute, and correlate these wavefields for all shots in order to obtain the desired image gathers. Therefore, the image gathers are typically only computed for a limited number of subsurface points and for a limited range of subsurface offsets, which may cause problems in complex geological areas with large geologic dips. We overcome increasing computational and storage costs of extended image volumes by introducing a formulation that avoids explicit storage and removes the customary and expensive loop over shots, found in conventional extended imaging. As a result, we end up with a matrix-vector formulation from which different

image gathers can be formed and with which amplitude-versus-angle and wave-equation migration velocity analyses can be performed without requiring prior information on the geologic dips. Aside from demonstrating the formation of two-way extended image gathers for different purposes and at greatly reduced costs, we also present a new approach to conduct automatic wave-equation based migration-velocity analysis. Instead of focussing in particular offset directions and preselected subsets of subsurface points, our method focuses every subsurface point for all subsurface offset directions using a randomized probing technique. As a consequence, we obtain good velocity models at low cost for complex models without the need to provide information on the geologic dips.

# INTRODUCTION

Seismic reflection data are a rich source of information about the subsurface and by studying both dynamic and kinematic properties of the data we can infer both large-scale velocity variations as well as local rock properties. While seismic data volumes – as a function of time, source and receiver positions – contains all necessary information, it is often more convenient to map the relevant events present in pre-stack data to their respective positions in the subsurface. This stripping away of the propagation effects leads to the definition of an *image volume* or *extended image* – as a function of depth, lateral position and some redundant spatial coordinate(s) – that has the same (or higher) dimensionality as the original data volume. This mapping can be thought of as a coordinate transform, depending on the large-scale background velocity model features, that maps reflection events observed in data collected at the surface to focussed secondary point sources tracing out the respective reflectors. The radiation pattern of these point sources reveals the angle-dependent reflection coefficient and can be used to infer the local rock properties. Errors in the large-scale background velocity model features are revealed through the failure of the events to fully focus. This principle forms the basis of many velocity-model analysis procedures.

Over the past decades various methods have been proposed for computing and exploiting image volumes or slices thereof – the so-called image gathers (Claerbout, 1970; Doherty and Claerbout, 1974; de Bruin et al., 1990; Symes and Carazzone, 1991; ten Kroode et al., 1994; Chauris et al., 2002; Biondi and Symes, 2004; Sava and Vasconcelos, 2011; Koren and Ravve, 2011). These approaches differ in the way the redundant coordinate is introduced and the method used to transform data volumes into image volumes. Perhaps the most well-known example are normal moveout corrected midpoint gathers, where simple move-

out corrections transform observed data into volumes that can be migrated into extended images that are a function of time, midpoint position and surface offset (Claerbout, 1985b).

While this type of surface-offset pre-stack images have been used for migration-velocity analysis and reservoir characterization, these extended images may suffer from unphysical artifacts. For this reason extended images are nowadays formed as functions of the subsurface offset, rather than surface offset as justified by Stolk et al. (2009), who showed that this approach produces artifact-free image gathers in complex geological settings. So far, wave-equation based constructions of these extended images are based on the double-square-root equation (Claerbout, 1970; Doherty and Claerbout, 1974; Biondi et al., 1999; Prucha et al., 1999; Brandsberg-Dahl et al., 2003; Kühl and Sacchi, 2003; Duchkov and Maarten, 2009), which produces image volumes as a function of depth and virtual subsurface source and receiver positions.

With the advent of reverse-time migration (Whitmore et al., 1983; Baysal et al., 1983; Levin, 1984), these one-way, and therefore angle-limited one-way approaches, are gradually being replaced by methods based on the two-way wave-equation, which is able to produce gathers as a function of depth and horizontal or vertical offset, or both (Biondi and Symes, 2004; Sava and Vasconcelos, 2011). This is achieved by forward propagating the source and backward propagating the data and subsequently correlating these source and receiver wavefields at non-zero offset/time lag. Depending on the extended imaging conditions (Sava and Biondi, 2004; Sava and Fomel, 2006), various types of subsurface extended image gathers can be formed by restricting the multi-dimensional cross-correlations between the propagated source and receiver wavefields to certain specified coordinate directions. The motivation to depart from horizontal offset only is that steeply dipping events do not optimally focus in the horizontal direction, even for a kinematically correct velocity model. A temporal shift

instead of a subsurface offset is sometimes also used as it is more computationally efficient MacKay and Abma (1992); Sava and Fomel (2006).

Up to this point, most advancements in image-gather based velocity-model building and reservoir characterization are due to improved sampling of the extended images and/or a more accurate wave propagators. However, these improvements carry a heavy price tag since the computations typically involve the solution of the forward and adjoint wave equation for each shot, followed by subsequent cross-correlations. As a result, computational and memory requirements grow uncontrollably and many practical implementations of subsurface offset images are therefore restricted, (e.g., by allowing only for lateral interaction over a short distance), and the gathers are computed for a subset of image points only. Unfortunately, the computational complexity of forming image gathers, as presented by Sava and Vasconcelos (2011), does not only scale with the costs of computing the correlations but also grow linearly with the number of sources. As a result, forming full subsurface extended image volumes rapidly becomes prohibitively expensive even for small two-dimensional problems.

Extended images play an important role in wave-equation migration-velocity analysis (WEMVA), where velocity model updates are calculated by minimizing an objective function that measures the coherency of image gathers (Symes and Carazzone, 1991; Shen and Symes, 2008). Regrettably, the computational and storage costs associated with this approach easily becomes unmanageable unless we restrict ourselves to a few judiciously chosen subsurface points (Yang and Sava, 2015). As a result, we end up with an expensive method, which needs to loop over all shot records and allowing for the computation of subsurface offset gathers for a limited number of subsurface points and directions. This is problematic because the effectiveness of WEMVA is impeded for dipping reflectors that do not focus as

well along horizontal offsets.

Extended images also serve as input to amplitude-versus-angle (AVA) or amplitude-versus-offset (AVO) analysis methods that derive from the (linearized) Zoeppritz equations (Aki and Richards, 1980). In this situation, the challenge is to produce reliable amplitude preserving angle/offset gathers in complex geological environments (see e.g., de Bruin et al. (1990); van Wijngaarden (1998); Rickett and Sava (2002); Sava and Fomel (2003); Kuhel and Sacchi (2003); Biondi and Symes (2004); Sava and Vasconcelos (2011); Bai et al. (2013)) from primaries only or, more recently from surface-related multiples, as demonstrated by Lu et al. (2014). In the latter case, good angular illumination can be obtained from conventional marine towed-streamer acquisitions with dense receiver sampling. As WEMVA, these amplitude analysis are biased when reflectors are dipping, calling for corrections dependent on geological dips that are generally unknown (Brandsberg-Dahl et al., 2003).

We present a new wave-equation based factorization principle that removes computational bottlenecks and gives us access to the kinematics and amplitudes of full subsurface offset extended images without carrying out explicit cross-correlations between source and receiver wavefields for each shot. We accomplish this by carrying out the correlations implicitly among all wavefields via actions of full extended image volumes on certain probing/test vectors. Depending on the choice of these probing vectors, these actions allow us to compute common-image-point (CIPs), common-image- (CIGs) and dip-angle gathers at certain predefined subsurface points in 2- and 3-D as well as objective functions for WEMVA. None of these require storage of wavefields and loops over shots.

The paper proceeds as follows. After introducing the governing equations of continuous-

space monochromatic extended image volumes, their relation to migrated images, CIPs and CIGs, we derive the two-way equivalent of the *double square-root equation* and move to a discrete setting that reveals a wave-equation based factorization of discrete full extended image volumes. Next, we show how this factorization can be used to extract information on local geological dips and radiation patterns for AVA purposes and how full offset extended image volumes can be used to carry out automatic WEMVA. Each application is illustrated by carefully selected stylized numerical examples in 2- and 3-D.

### Notation

In this paper, we use lower/upper case letters to represents scalars, e.g., $x_m, R$, and lower case boldface letters to represents vectors (i.e. one-dimensional quantities), e.g., $\mathbf{x}, \mathbf{x}'$. We denote matrices and tensors using upper case boldface letters, e.g., $\mathbf{E}, \widetilde{\mathbf{E}}, \mathbf{R}$. Subscript $i$ represents frequencies, $j$ represents the number of sources and/or receivers and $k$ represents the subsurface grid points. 2-D represents seismic volumes with one source, one receiver, and time dimensions. 3-D represents seismic volumes with two sources, two receivers, and time dimensions.

## ANATOMY & PHYSICS

Before describing the proposed methodology of extracting information from full subsurface-offset extended image volumes using the proposed probing technique, we first review the governing equations. We denote the full-extended image volumes as

$$e(\omega, \mathbf{x}, \mathbf{x}') = \int_{\mathcal{D}_s} \mathrm{d}\mathbf{x}_s \; u(\omega, \mathbf{x}, \mathbf{x}_s)\overline{v(\omega, \mathbf{x}', \mathbf{x}_s)}, \tag{1}$$

where the overline denotes complex conjugation, $u$ and $v$ are source and receiver wavefields as a function of the frequency $\omega \in \Omega \subset \mathbb{R}$, subsurface positions $\mathbf{x}, \mathbf{x}' \in \mathcal{D} \subset \mathbb{R}^n$ ($n = 2$ or 3) and source positions $\mathbf{x}_s \in \mathcal{D}_s \subset \mathbb{R}^{n-1}$. These monochromatic wavefields are obtained by solving

$$H(m)u(\omega, \mathbf{x}, \mathbf{x}_s) = q(\omega, \mathbf{x}, \mathbf{x}_s), \tag{2}$$

$$H(m)^* v(\omega, \mathbf{x}, \mathbf{x}_s) = \int_{\mathcal{D}_r} \mathrm{d}\mathbf{x}_r \; d(\omega, \mathbf{x}_r, \mathbf{x}_s)\delta(\mathbf{x} - \mathbf{x}_r), \tag{3}$$

where $H(m) = \omega^2 m(\mathbf{x})^2 + \nabla^2$ is the Helmholtz operator with Sommerfeld boundary conditions, the symbol $^*$ represents the conjugate-transpose (adjoint), $m$ is the squared slowness, $q$ is the source function and $d$ represents the reflection-data at receiver positions $\mathbf{x}_r \in \mathcal{D}_r \subset \mathbb{R}^{n-1}$.

Equations (1-3) define a linear mapping from a $2n-1$ dimensional data volume $d(\omega, \mathbf{x}_r, \mathbf{x}_s)$ to a $2n+1$ dimensional image volume $e(\omega, \mathbf{x}, \mathbf{x}')$. Conventional migrated images are obtained by applying the zero-time/offset imaging condition (Sava and Vasconcelos, 2011)

$$r(\mathbf{x}) = \int_{\Omega} \mathrm{d}\omega \; e(\omega, \mathbf{x}, \mathbf{x}). \tag{4}$$

Once we have the full extended image, we can extract all conceivable image and angle gathers by applying appropriate imaging conditions (Sava and Vasconcelos, 2011). For instance, conventional 2-D common-image-gathers (CIGs), as a function of lateral positions $x_m$, depth $z$ and horizontal offset $h_x$ are defined as

$$I_{\mathrm{CIG}}(z, h; x_m) = \int_{\Omega} \mathrm{d}\omega \; e\left(\omega, (x_m - h_x, z)^T, (x_m + h_x, z)^T\right), \tag{5}$$

where $^T$ denotes the transpose.

Similarly, time-shifted common-image-point (CIP) gathers at subsurface points $\mathbf{x}_k$, as a

function of all spatial offset vectors $\mathbf{h}$ and temporal shifts $\Delta t$ becomes

$$I^{\text{ext}}_{\text{CIP}}(\mathbf{h}, \Delta t; \mathbf{x}_k) = \int_{\Omega} \mathrm{d}\omega \; e(\omega, \mathbf{x}_k, \mathbf{x}_k + \mathbf{h}) e^{\imath\omega\Delta t}, \tag{6}$$

where $\imath = \sqrt{-1}$. Note that we departed in this expression from the usual symmetric definition $e(\omega, \mathbf{x}_k - \mathbf{h}, \mathbf{x}_k + \mathbf{h})$ because it turns out to be more natural for our shot-based computations. Because we consider these gathers of full-subsurface offset only, we apply a zero-time imaging condition to the CIPs–i.e., $I_{\text{CIP}}(\mathbf{h}; \mathbf{x}_k) = I^{\text{ext}}_{\text{CIP}}(\mathbf{h}, \Delta t = 0; \mathbf{x}_k)$. These gathers form the theoretical basis for AVA and WEMVA.

Moving to a discrete setting, we have $N_s$ sources $\{\mathbf{x}_{s,j}\}_{j=1}^{N_s} \in \mathcal{D}_s$, $N_r$ receivers $\{\mathbf{x}_{r,j}\}_{j=1}^{N_r} \in \mathcal{D}_r$, $N_f$ frequencies $\{\omega_i\}_{i=1}^{N_f} \in \Omega$ and discretize the domain $\mathcal{D}$ using a rectangular grid with a total of $N_x$ grid points $\{\mathbf{x}_k\}_{k=1}^{N_x}$. We organize the source and receiver wavefields in tensors of size $N_f \times N_x \times N_s$ with elements $u_{ikj} \equiv u(\omega_i, \mathbf{x}_k, \mathbf{x}_{s,j})$ and $v_{ikj} \equiv v(\omega_i, \mathbf{x}_k, \mathbf{x}_{s,j})$. For the $i^{\text{th}}$ frequency, we can represent the wavefields for all sources as complex valued $N_x \times N_s$ matrices $\mathbf{U}_i$ and $\mathbf{V}_i$, where each column of the matrix represents a monochromatic source experiment.

Full $2n + 1$ dimensional image volumes can now be represented as a 3-D tensor with elements $e_{ikk'} \equiv e(\omega_i, \mathbf{x}_k, \mathbf{x}_{k'})$. A slice through this tensor at frequency $i$ is an $N_x \times N_x$ matrix, which can be expressed as an outer product of the matrices $\mathbf{U}_i$ and $\mathbf{V}_i$

$$\mathbf{E}_i = \mathbf{U}_i \mathbf{V}_i^*, \tag{7}$$

where $^*$ denotes the complex conjugate transpose. The matrix $\mathbf{E}_i$ is akin to Berkhout's *reflectivity matrices* (Berkhout, 1993), except that $\mathbf{E}_i$ captures vertical interactions as well since it is derived from the two-way wave-equation. These source and receiver wavefields

obey the following discretized Helmholtz equations:

$$\mathbf{H}_i(\mathbf{m})\mathbf{U}_i = \mathbf{P}_s^*\mathbf{Q}_i, \tag{8}$$

$$\mathbf{H}_i(\mathbf{m})^*\mathbf{V}_i = \mathbf{P}_r^*\mathbf{D}_i, \tag{9}$$

where $\mathbf{H}_i(\mathbf{m})$ represents the discretized Helmholtz operator for frequency $\omega_i$ with absorbing boundary conditions and for a gridded squared slowness $\mathbf{m}$. The $N_s \times N_s$ matrix $\mathbf{Q}_i$ represents the sources (i.e., each column is a source function), the $N_r \times N_s$ matrix $\mathbf{D}_i$ contains reflection-data (i.e., each column is a monochromatic shot gather after subtraction of the direct arrival) and the matrices $\mathbf{P}_s, \mathbf{P}_r$ sample the wavefields at the source and receiver positions (and hence, their transpose injects the sources and receivers into the grid). Remark that these are the discretized versions of equations (2, 3).

Substituting relations (8, 9) into the definition of the extended image (7) yields

$$\mathbf{H}_i\mathbf{E}_i\mathbf{H}_i = \mathbf{P}_s^*\mathbf{Q}_i\mathbf{D}_i^*\mathbf{P}_r. \tag{10}$$

This defines a natural 2-way analogue of the well-known double-square-root equation. From equation (10), we derive the following expression for monochromatic full extended image volumes

$$\mathbf{E}_i = \mathbf{H}_i^{-1}\mathbf{P}_s^*\mathbf{Q}_i\mathbf{D}_i^*\mathbf{P}_r\mathbf{H}_i^{-1}, \tag{11}$$

which is a discrete analogue of the linear mapping from data to image volumes defined in equations (1-3). Note that for co-located sources and receivers ($\mathbf{P}_r = \mathbf{P}_s$) and ideal discrete point sources ($\mathbf{Q}$ is the identity matrix) we find that $\mathbf{E}$ is complex symmetric (i.e., $\Re(\mathbf{E}^*) = \Re(\mathbf{E})$ and $\Im(\mathbf{E}^*) = -\Im(\mathbf{E})$) because of source-receiver reciprocity.

The usual zero-time/offset imaging conditions translate to

$$\mathbf{r} = \sum_{i=1}^{N_f} \mathrm{diag}(\mathbf{E}_i), \tag{12}$$

where $\mathbf{r}$ is the discretized reflectivity and $\mathsf{diag}(\mathbf{A})$ denotes the diagonal elements of $\mathbf{A}$ organized in a vector. Various image gathers are embedded in our extended image volumes as illustrated in Figure 1.

As we will switch between continuous and discrete notation throughout the paper, the correspondence between the image volume $e(\omega, \mathbf{x}, \mathbf{x}')$ and the matrices $\mathbf{E}_i$ is listed in Table 1. For simplicity, we will drop the frequency-dependence from our notation for the remainder of the paper and implicitly assume that all quantities are monochromatic with the understanding that all computations can be repeated as needed for multiple frequencies. We will also assume that the zero-time imaging condition is applied by summing over the frequencies, followed by taking the real part. We further note that full extended image volumes can be severely aliased in case of insufficient source-receiver sampling. Therefore, one would in practice only extract gathers from image volumes in well-sampled directions.

## COMPUTATIONAL ASPECTS

Of course, we can never hope to explicitly form the complete image volumes owing to the enormous computational and storage costs associated with these volumes that are quadratic in the number of gridpoints $N_x$. In particular, we will discuss the computation of monochromatic image volumes $\mathbf{E}_i$ and drop the subscript $i$ in the remainder of the section.

To avoid forming extended images $\mathbf{E}$ explicitly, we instead propose to probe these volumes by right-multiplying them with $N_x \times K$ sampling matrices $\mathbf{W} = [\mathbf{w}_1, \ldots, \mathbf{w}_K]$, where $K$ denotes the number of samples and $\mathbf{w}_k$ denotes a single probing or sampling vector. After sampling, the reduced image volume $\widetilde{\mathbf{E}}$ now reads

$$\widetilde{\mathbf{E}} = \mathbf{E}\mathbf{W} = \mathbf{H}^{-1}\mathbf{P}_s^*\mathbf{Q}\mathbf{D}^*\mathbf{P}_r\mathbf{H}^{-1}\mathbf{W}. \tag{13}$$

Our main contribution is that we can compute these compressed volumes efficiently with algorithm 1 or 2. As one can see, these computations derive from wave-equation based factorizations that avoid storage and loops over all shots.

**Algorithm 1** Compute matrix-vector multiplication of image volume matrix with given vectors $\mathbf{W} = [\mathbf{w}_1, \ldots, \mathbf{w}_K]$. The computational cost is $2N_s$ wave-equation solves plus the cost of correlating the wavefields.

compute all the source wavefields $\mathbf{U} = \mathbf{H}^{-1}\mathbf{P}_s^*\mathbf{Q}$,

compute all the receiver wavefields $\mathbf{V} = \mathbf{H}^{-*}\mathbf{P}_r^*\mathbf{D}$

compute weights $\widetilde{\mathbf{Y}} = \mathbf{V}^*\mathbf{W}$

compute the product $\widetilde{\mathbf{E}} = \mathbf{U}\widetilde{\mathbf{Y}}$.

**Algorithm 2** Compute matrix-vector multiplication of image volume matrix with given vectors $\mathbf{W} = [\mathbf{w}_1, \ldots, \mathbf{w}_K]$. The computational cost is $2K$ wave-equation solves plus the cost of correlating the data matrices.

compute $\widetilde{\mathbf{U}} = \mathbf{H}^{-1}\mathbf{W}$ and sample this wavefield at the receiver locations $\widetilde{\mathbf{D}} = \mathbf{P}_r\widetilde{\mathbf{U}}$;

correlate the result with the data $\widetilde{\mathbf{W}} = \mathbf{D}^*\widetilde{\mathbf{D}}$ to get the source weights;

use the source weights to generate the simultanoues sources $\widetilde{\mathbf{Q}} = \mathbf{Q}\widetilde{\mathbf{W}}$;

compute the resulting wavefields $\widetilde{\mathbf{E}} = \mathbf{H}^{-1}\mathbf{P}_s^*\widetilde{\mathbf{Q}}$.

While both algorithms produce the same compressed image volume, Algorithm 1 corresponds to the traditional way of computing image volumes where *all* source and receiver wavefields are computed first and subsequently cross-correlated. Algorithm 2, on the other hand, produces *exactly* the same result without looping over all shots and without carrying out explicit cross-correlations. It arrives at this result by cross-correlating the data and source wavefields and by solving only two wave-equations per probing vector instead of solving the forward and adjoint wave-equations for each shot. This means that our method

(Algorithm 2) gains computationally as long as the number of probings is small compared to the number of sources ($K < N_s$). The choice of the probing vectors depends on the application.

For completeness, we summarized the computational complexities of the two schemes in Table 2 in terms of the number of sources $N_{\mathrm{s}}$, receivers $N_{\mathrm{r}}$, subsurface sample points $N_x$ and desired number of subsurface offsets in each direction $N_{h_{\{x,y,z\}}}$.

## CASE STUDY 1: COMPUTING GATHERS

We now describe how common-image-point gathers (CIPs) and common-image-gathers (CIGs) can be formed with Algorithm 2.

**CIPs:** According to Algorithm 2, a CIP at midpoint $\mathbf{x}_k$ can be computed efficiently by extracting the corresponding column from the monochromatic matrix $\mathbf{E}$ representing the full extended image. We achieve this at the cost of only two wave-equation solves by setting $\mathbf{w}_k$ to a cardinal basis vector with its non-zero entry corresponding to the location of a single point source at $\mathbf{x}_k$. Because of the proposed factorization, the number of required wave-equation solves is reduced from twice the number of shots to only two per subsurface point, representing an order-of-magnitude improvement. As long as the number of subsurface points are not too large, this reduction allows for targeted quality control with omnidirectional extended image gathers.

For reasonable background velocity models, we can even compute these image gathers simultaneously as long as the corresponding subsurface points are spatially separated. In this case, the probing vectors $\mathbf{w}_k$ correspond to simultaneous subsurface sources without encoding. As a result, we may introduce cross-talk in the gathers, but expect

that there will be very little interference when the locations being probed are sufficiently far away from each other. Even though this cross-talk may interfere with the ability to visually inspect the CIPs, we will see that these interferences can be rendered into incoherent noise via randomized source encoding as shown by van Leeuwen et al. (2011) for full waveform inversion (FWI), a property we will later use in automated migration-velocity analyses.

**CIGs** We can also extract common-image-gather at a lateral position $x_k$ by (densely) sampling the image volumes at $\mathbf{x}_k = (x_k, z_k)^T$ at all depth levels. In this configuration, the sampling matrix takes the form $\mathbf{W} = \mathbf{W}_x \otimes \mathbf{W}_z$, where $\mathbf{W}_x = (0, 0, \ldots, 1, \ldots, 0)^T$ is a cardinal basis vector as before with a single non-zero entry located at the index corresponding to the midpoint position $x_k$ and $\mathbf{W}_z = \mathbf{I}$ is the identity matrix, sampling all gridpoints in the vertical direction. The resulting gathers $\widetilde{\mathbf{E}} = \mathbf{EW}$ are now a function of $(z, \Delta x, \Delta z)$ and contain both vertical and lateral offsets. We can form conventional image gathers by extracting a slice of the volume at $\Delta z = 0$. The computational cost per CIG in 2-D are roughly the same as the conventionally computed CIGs; $2N_z$ vs. $2N_s$ wave-equation solves, where $N_z$ denotes the number of samples in depth. In 3-D however, the proposed way of computing the gathers via algorithm 2 is a order of magnitude faster because the number of sources in a 3-D seismic acquisition is an order of magnitude bigger while the number of samples in depth stays the same.

As with the CIPs, we can generate these gathers simultaneously, by sampling various lateral positions at the same time for each depth level.

## Numerical results in 2-D

To illustrate the discussed methodology, we compute various gathers on a central part of Marmousi model. We use a gridspacing of 10 m, 81 co-located sources and receivers with 50 m spacing and frequencies between 5 and 25 Hz with 0.5 Hz spacing. The source wavelet is a Ricker wavelet with a peak frequency of 15 Hz. The wavefields are modeled using a 9-point finite difference discretization of the Helmholtz operator with a sponge boundary condition. The direct wave is removed prior to computing the image gathers.

Figure 2 shows the migrated image for wrong (a) and correct background velocity models (b). At three locations indicated by the $*$ symbol we extract the CIP gathers, shown in (c) for a background velocity model that is too low and in (d) for the correct velocity. As a result of the cross-correlations between various events in propagated wavefields several spurious events are present so the recovered CIP gathers are only meaningful for interpretation close to the image point. However, as expected most of the energy concentrates along the normal to the reflector. We can generate these three CIPs *simultaneously* at the cost of generating one CIP by defining the sampling vector $\mathbf{w}_k$ to represent the three point sources simultaneously. As we mentioned before, this may result in cross-talk between the CIPs, however, in this case the events do not significantly interfere because the events are separated laterally, as shown in Figure 2 (c,d).

To illustrate the benefits of the proposed scheme, we also report the computational time (in sec) and memory (in MB) required to compute a single common-image point gather using Algorithm 1 and 2. The results are shown in Table 3. We can see that even for a small toy model, the probing technique reduces the computational time and memory requirement by a factor of 20 and 30, respectively.

Finally, Figures 2 (e-f) contain CIGs at two lateral positions for a background velocity that is too low (e) and correct (f). In this example, we generated the image volume for each depth level simultaneously for all lateral positions. When creating many gathers, such a simultaneous probing can substantially reduce the required computational cost.

## Numerical results in 3-D

Notwithstanding the achieved speedup and memory reduction in 2-D, the proposed probing method outlined in Algoritm 2 is a true enabler in 3-D where there is no realistic hope to store full extended image volumes whose size is quadratic in the number of gridpoints $N_x$. Besides, the number of sources also becomes quadratic for full-azimuth acquisitions. As in the 2-D case, our probing technique is a key enabler allowing us to compute CIPs without allocating exorbitant amounts of memory and computational resources. To illustrate our claim, we compute a single CIP for the Compass velocity model provided to us by BG Group. Figures 3, 4 contains both vertical and lateral cross-sections of this complicated 3D velocity model, which contains $131 \times 101 \times 101$ gridpoints. The model is 780 m deep and 2.5 km across in both lateral directions.

We generated data from this velocity model following an ocean-bottom node configuration where sources are placed at the water surface along the $x$ and $y$ directions with a sampling interval of 75 m. The receivers are placed at the sea bed with a sampling of 50 m resulting in a data volume with 1156 sources and 2601 receivers. We generated this marine data volume with a 3-D time-harmonic Helmholtz solver, based on a 27 point discretization, perfectly-matching boundary conditions, and a Ricker wavelet with a central frequency of 15 Hz. During the simulations and imaging, we used 15 frequencies ranging from 5 to 12 Hz

with a sampling interval of 0.5 Hz. For further details on the employed wave-equation solver, we refer to Lago et al. (2014); van Leeuwen and Herrmann (2014).

Figures 3b and 5 show an example of a full CIP gather extracted at $z = 390$, $x = 1250$ and $y = 1250$ m. Aside from behaving as expected, the observed running time with Algorithm 2 is 1500 times faster compared to the corresponding time needed by Algorithm 1. While Algorithm 1 and 2 lend themselves well for parallelization over frequencies, shots, and probing vectors, our method avoids a loop over 1156 shots while avoiding explicit formation of extended image that would require the allocation of a matrix with $101^6$ entries.

## CASE STUDY 2: DIP-ANGLE GATHERS

Aside from their use for kinematical quality control during velocity model building, common-image gathers (CIGs) also contain dynamic amplitude-versus-angle (AVA) information on reflecting interfaces that can serve to invert associated rock properties (Mahmoudian and Margrave, 2009). For this purpose, various definitions of angle-domain CIGs have been proposed (de Bruin et al., 1990; van Wijngaarden, 1998; Rickett and Sava, 2002; Sava and Fomel, 2003; Kuhel and Sacchi, 2003; Biondi and Symes, 2004; Sava and Vasconcelos, 2011). Extending the work of de Bruin et al. (1990) to include corrections for the geological dip $\theta$, we extract angle-dependent reflection coefficients from a subsurface point $\mathbf{x}_0$ by evaluating the following integral:

$$R(\mathbf{x}_0, \alpha; \theta) \propto \int_\Omega \mathrm{d}\omega \int_{-h_{\max}}^{h_{\max}} \mathrm{d}h \;\; e(\omega, \mathbf{x}_0, \mathbf{x}_0 + h\mathbf{n}(\theta)^\perp) e^{\imath\omega \sin(\alpha) h / v(\mathbf{x})} \tag{14}$$

over frequencies and offsets. We use the $\propto$ symbol to indicate that this expression holds up to proportionality constant.

In this expression, $\alpha$ is the angle of incidence with respect to the normal (see Figure

6), $v(\mathbf{x})$ is the local background velocity used to convert subsurface offsets to angles, and $\mathbf{n}(\theta)^{\perp}$ denotes the tangent vector to the reflector defining the offset vector in this direction ($h\mathbf{n}(\theta)^{\perp}$). The integral is carried out over the effective offset range denoted by $h_{\max}$, which decreases for deeper parts of the model. The integral over frequencies correspond to the zero-time imaging condition. As illustrated in Figure 6, the normal $\mathbf{n}(\theta) = (\sin\theta, \cos\theta)^T$ and tangent vectors to a reflecting interface depend on the geological dip $\tau$, which is unknown in practice. Unfortunately, ignoring this factor may lead to erroneous amplitudes in cases where this dip is steep. This means that we need to extract CIGs, following the procedure outlined above, as well as estimates on the geological dip from the extended image volumes.

Following Brandsberg-Dahl et al. (2003), we use the stack power to estimate the geological dip at subsurface point $\mathbf{x}_k$ via

$$\widehat{\theta} = \arg\max_{\theta} \int_{-h_{\max}}^{h_{\max}} \mathrm{d}h \quad \left| \int_{\Omega} \mathrm{d}\omega \; e(\omega, \mathbf{x}, \mathbf{x}_k + h\mathbf{n}(\theta)) \right|^2 . \tag{15}$$

This maximization is based on the assumption that the above integral attains a maximum value when we collect energy from the image volume at time zero and along a direction that corresponds to the true geologic dip. Both integrals in equation 14 and 15 require information on monochromatic extended image volumes at subsurface position $\mathbf{x}_k$ only–i.e., $e(\omega, \mathbf{x}_k, \mathbf{x}')$ for $\omega \in \Omega$, to which we have readily access via probing as described in Algorithm 2. The resulting gathers $e(\omega, \mathbf{x}_k, \mathbf{x}')$ contain the required information to estimate local geologic-dip corrected angle-dependent reflection coefficient $R(\alpha; \mathbf{x}_k, \widehat{\theta})$ where the correction is carried with dip estimate $\widehat{\theta}$ that maximizes the stack power. Since we have access to all subsurface offsets at no additional computational costs, there is no need to select a maximum subsurface offsets $h_{\max}$ priori even though the effective subsurface offset decreases with depth.

## Numerical results

To illustrate the proposed method of computing angle-domain common-image gathers (CIGs), we compare the modulus for plotting reasons of the estimated reflection coefficients $|R(\alpha; \mathbf{x}_k, \theta_k)|$ with the theoretical PP-reflection coefficients predicted by the Zoeppritz equations (Koefoed, 1955; Shuey, 1985).

To make this comparison, we used a finite-difference time-domain acoustic modelling code (Symes et al., 2011) to generate three synthetic data sets for increasingly complex models, namely a two-layer velocity and constant density model (Figures 7 (a, b)); a four layer model with properties taken from de Bruin et al. (1990) (Figures 8 (a,b)), and a two layer lateral varying velocity and density model–i.e., one-horizontal reflector and one-dipping reflector (Figures 9(a, b)). The purpose of these three experiments is to (i) verify the velocity-change-only angle dependent reflection coefficients; (ii) study the effects of density and decreasing effective horizontal offset with depth; and (iii) illustrate the effect of the geologic dip on the reflection coefficients. We used a Ricker wavelet with a peak frequency of 15 Hz as a source signature. In all three examples, seismic data is simulated using split-spread acquisition. The gathers used in the AVA analyses are obtained using Algorithm 2 and discrete version of equations 14 and 15 for a smoothed version of the layered velocity models.

The estimated angle-dependent reflection coefficients for the first model is displayed in Figure 7 (c). We can see that these estimates, extracted from our extended image volumes, match the theoretical reflection coefficients according to the Zoeppritz equations after a single amplitude scaling fairly well up to angles of 50° that are reasonably close to effective aperture angle (depicted by the black line in the Figures of the AVA curves). Beyond these

angles, the Zoeppritz equations are no longer accurate. The results for the deeper four layer model depicted in Figures 8 (c, d, e, f) clearly show the imprint of smaller horizontal offsets with depth. From the AVA plots in Figure 8, we can observe that the reflection coefficients for the first and second reflector are well matched up to 50° and 40° and, for the third and fourth reflectors, to only 20°. We also confirm that that the angle-dependent reflection coefficient associated with a changes in density is approximately flat (see Figure 8 (e)). The finite aperture of the data accounts for the discrepancy beyond these angles.

To illustrate our method's ability to correct for the geological dip, we consider a common-image-point (CIP) gather at $x = 2250$ m and $z = 960$ m. As we can see from Figure 9 (c), this CIP is well focused and with the local geologic dip of the reflector. The corresponding stack power is plotted in Figure 9 (d), which attains maximum power at $\widehat{\theta} = 10.8°$ an estimate close to the actual dip of 11°. To demonstrate the effect of ignoring the geological dip when computing angle gathers, we evaluate equation 14 for $\theta = 0$. The results included in Figure 10 clearly illustrate the benefit of incorporating the dip-information in angle-domain image gathers as it allows for a more accurate estimation of the angle-dependent reflection coefficients. This experimental result supports our claim that proposed extended image volume framework lends itself well to estimate geologic-dip corrected angle gathers. As we mentioned before, the proposed method also reaps the computational benefits of probing extended image volumes as outlined in Algorithm 2.

## CASE STUDY 3: WAVE-EQUATION MIGRATION-VELOCITY ANALYSIS (WEMVA)

Aside from providing localized information on the kinematics and dynamics, full subsurface offset extended image volumes also lend themselves well for automatic velocity analyses that minimize some global focusing objective (Symes and Carazzone, 1991; Biondi and Symes, 2004; Shen and Symes, 2008; Sava and Vasconcelos, 2011; Mulder, 2014; Yang and Sava, 2015). For this reason, wave-equation migration-velocity analysis (WEMVA) can be considered as another important application where subsurface image gathers are being used extensively. In this case, the aim is to build kinematically correct background velocity models that either promote similarity amongst different surface offset gathers, as in the original work by Symes and Carazzone (1991) on Differential Semblance, or that aim to focus at zero subsurface offset, an approach promoted by recent work on WEMVA (Brandsberg-Dahl et al., 2003; Shen and Symes, 2008; Symes, 2008b). While these wave-equation based methods are less prone to imaging artifacts Stolk and Symes (2003), they are computationally expensive restricting the number of directions in which the subsurface offsets can be calculated. This practical limitation may affect our ability to handle unknown geological dips (Sava and Vasconcelos, 2011; Yang and Sava, 2015).

Before presenting an alternative approach that overcomes these practical limitations, let us first formulate an instance of WEMVA, based on the probing technique outlined in Algorithm 2. In this discrete case, WEMVA corresponds to minimizing

$$\min_{\mathbf{m}} \sum_{k=1}^{N_x^2} \|\mathbf{S}_k \overline{\mathbf{E}}(\mathbf{m}) \mathbf{w}_k\|_2^2, \tag{16}$$

with $\overline{\mathbf{E}}(\mathbf{m}) = \sum_{i \in \Omega} \mathbf{E}_i(\mathbf{m})$. As before the $\mathbf{E}_i(\mathbf{m})$'s denote monochromatic extended image volumes for the background velocity model $\mathbf{m}$. With this definition, we absorb both the

zero-time imaging condition, by summing over frequencies. The vector $\mathbf{w}_n$ represents a point-source at a subsurface point corresponding to the $k^{\text{th}}$ entry of $\mathbf{w}$. We compute this sum efficiently via first probing the each monochromatic extended image volumes with the vector $\mathbf{w}_k$ followed by sum over frequency instead of summing over the monochromatic full subsurface image volumes followed by probing with the vector $\mathbf{w}_k$. Finally, the diagonal matrix $\mathbf{S}_k$ penalizes defocussed energy by applying a weighting function. Often, this weight is chosen proportional to the lateral subsurface offset (Shen and Symes, 2008). The main costs of this approach (cf. equation 16) are formed by the number of gathers, which equals the number of grid points. Of course, WEMVA is conducted in practice with a subset of grid points $N_x$, the number of which depends on the complexity of the subsurface.

To arrive at an alternative more cost effective formulation that offers flexibility to focus in all offset directions, we take a different tack by using the fact that focussed extended image volumes commute with diagonal weighting matrices (Kumar et al., 2013; Symes, 2014) that penalize off-diagonal energy–i.e., we have

$$\overline{\mathbf{E}}\,\mathrm{diag}(\mathbf{s}) \approx \mathrm{diag}(\mathbf{s})\,\overline{\mathbf{E}} \tag{17}$$

for a given weighting vector $\mathbf{s}$. For the specific case where the entries in $\mathbf{s}$ correspond to lateral positions for each grid point in the model, forcing the above commutation relation corresponds to the objective of equation 16 with weights proportional to the horizontal subsurface offset. However, other options are also available including focusing in all offset directions. The optimization problem can now be written as

$$\min_{\mathbf{m}} \left\{ \phi(\mathbf{m}) = ||\overline{\mathbf{E}}(\mathbf{m})\mathrm{diag}(\mathbf{s}) - \mathrm{diag}(\mathbf{s})\overline{\mathbf{E}}(\mathbf{m})||_F^2 \right\}, \tag{18}$$

where $||\mathbf{A}||_F^2 = \sum_{i,j} a_{i,j}^2$ denotes the Frobenius norm. Minimization of this norm forces $\overline{\mathbf{E}}$ to focus as a function of the velocity model $\mathbf{m}$.

For obvious reasons, this formulation is impractical because even in 2-D we can not hope to store the extended image volumes $\overline{\mathbf{E}}$, whose size is quadratic in the number of grid points – $\overline{\mathbf{E}}$ is a $N_x^2 \times N_x^2$ matrix. However, we can still minimize the above objective function via random-trace estimation (Avron and Toledo, 2011), a technique that also underlies phase encoding techniques in full-waveform inversion van Leeuwen et al. (2011). With this technique, equation 18 can be evaluated to arbitrary accuracy via actions of $\overline{\mathbf{E}}$ on random vectors $\mathbf{w}$. With this approximation, the WEMVA objective becomes

$$\phi(\mathbf{m}) \approx \widetilde{\phi}(\mathbf{m}) = \frac{1}{K}\sum_{k=1}^{K} \|\mathbf{R}(\mathbf{m})\mathbf{w}_k\|_2^2, \tag{19}$$

where $\mathbf{R}(\mathbf{m}) = \overline{\mathbf{E}}\,(\mathbf{m})\mathrm{diag}(\mathbf{s}) - \mathrm{diag}(\mathbf{s})\,\overline{\mathbf{E}}(\mathbf{m})$. While other choices are possible, we select the $\mathbf{w}_k$ as Gaussian vectors with independent, identically distributed random entries with zero mean and unit variance. For this choice, $\widetilde{\phi}(\mathbf{m})$ and $\phi(\mathbf{m})$ are equal in expectation, which means that the above sample average is unbiased (van Leeuwen et al., 2011; Haber et al., 2012). As we know from source-encoding in full-waveform inversion (Krebs et al., 2009; van Leeuwen et al., 2011; Haber et al., 2012), good approximations can be obtained for small sample size $K \ll N_x$. We will study the quality of this approximation below.

The gradient of the approximate objective is given by

$$\nabla\widetilde{\phi}(\mathbf{m}) = \frac{1}{K}\sum_{k=1}^{K}\big(\nabla\overline{\mathbf{E}}(\mathbf{m}, \mathrm{diag}(\mathbf{s})\mathbf{w}_k) - \mathrm{diag}(\mathbf{s})\nabla\overline{\mathbf{E}}(\mathbf{m}, \mathbf{w}_k)\big)^*\mathbf{R}(\mathbf{m})\mathbf{w}_k, \tag{20}$$

where

$$\nabla\overline{\mathbf{E}}(\mathbf{m}, \mathbf{y}) = \frac{\partial\overline{\mathbf{E}}(\mathbf{m})\mathbf{y}}{\partial\mathbf{m}}$$

is the Jacobian of $\overline{\mathbf{E}}(\mathbf{m})\mathbf{y}$. We do not form this Jacobian matrix explicitly, but instead compute its action on a vector as follows:

$$\nabla\overline{\mathbf{E}}(\mathbf{m}, \mathbf{y})\delta\mathbf{m} \;\; = \;\; -\omega^2\left(\overline{\mathbf{E}}(\mathbf{m})\mathrm{diag}(\widetilde{\mathbf{y}}) + \mathbf{H}(\mathbf{m})^{-1}\mathrm{diag}(\widetilde{\mathbf{e}})\right)\delta\mathbf{m} \tag{21}$$

where $\widetilde{\mathbf{w}} = \mathbf{H}(\mathbf{m})^{-1}\mathbf{y}$, $\widetilde{\mathbf{e}} = \overline{\mathbf{E}}(\mathbf{m})\mathbf{y}$. The computation of the action of the adjoint of the Jacobian follows naturally.

We can now employ an iterative gradient-based method to find a minimizer of $\phi(\mathbf{m})$ by using a $K$-term approximation of this objective and its gradient (van Leeuwen et al., 2011; Haber et al., 2012). To remove possible bias from using a fixed set of random probing vectors, we redraw these vectors after each gradient update. Remaining errors can be controlled by increasing $K$ (Haber et al., 2012; Friedlander and Schmidt, 2012; van Leeuwen and Herrmann, 2014).

## Numerical results

We test the proposed wave-equation migration-velocity analysis (WEMVA) formulation on synthetic examples, illustrating the efficacy of the probing techniques. In all experiments, we use a 9-point finite-difference discretization of the 2-D Helmholtz equation to simulate the wavefields. The direct wave is removed from the data prior to performing the velocity analysis. To regularize the inversion, we parameterize the model using cubic B-splines (Symes, 2008a). We solve the resulting optimization problem with the limited-memory Broyden-Fletcher-Goldfarb-Shanno (L-BFGS) method (Nocedal and Wright, 2000).

*Need for full subsurface-offset image volumes*

Our first experiment is designed to illustrate the main benefit of working with full subsurface offsets in all directions in situations where both horizontal and vertical reflectors are present (Figure 11 (a) adapted from (Yang and Sava, 2015)). For this purpose, we juxtapose the focussing, for a velocity model with the correct kinematics, of common-image gathers

(CIGS) against focussing with common-image point gathers (CIPs) for a model with vertical and horizontal horizontal. While both CIG and CIP gathers can be used to form WEMVA objectives, their performance can be quite different. Ideally, CIGs measure focusing along offsets in the direction of the geologic dip for subsurface points sampled along spatial coordinated perpendicular to this direction, denoted by the yellow lines in Figure 11 (a). The green dots denote the location of the selected CIPs.

Since prior knowledge of geologic dips is typically not available, why not device a WEMVA scheme that focusses in all spatial directions? In that way, we are guaranteed to focus as illustrated in Figure 11 (b-d), for the horizontal reflector, and in Figure 11 (e-g) for the vertical reflector. From these figures it is clear that CIGs do not focus (Figure 11 (c,e)), despite the fact that the velocity model is correct. This lack of focusing may lead to erroneous biases during CIG-based WEMVA, a problem altogether avoided when we work with CIPs (Figure 11 (d,f)). Because CIPs are sensitive to focusing in all directions, there is no need to focus in time (Sava and Vasconcelos, 2011). While the advantages of CIP-based WEMVA are clear, we cheated by selecting CIPs on top of the reflecting interfaces, whose position is also generally not known in advance. This is where the randomized sampling comes to our rescue. By treating all subsurface points as random amplitude encoded sources, we will be able to form a CIP-based WEMVA objective, which does not require explicit knowledge on the location of the reflecting interfaces.

*Quality of the stochastic approximation*

As with FWI, randomly encoded sources—e.g. via random Gaussian weights, provide a vehicle to approximate (prohibitively) expensive to evaluate wave-equation based objectives

(cf. equations 18 and 19) to controllable accuracy by increasing $K$. Following Haber et al. (2012), we evaluate for a small subset (Figure 12 (a)) of the Marmousi model (Bourgeois et al., 1991) the true $\phi(\mathbf{m}_0 + \alpha\delta\mathbf{m})$ (solid blue line) and approximate $\tilde{\phi}(\mathbf{m}_0 + \alpha\delta\mathbf{m})$ (denoted by the error bars) objectives as a function of $\alpha$ in the direction of the gradient—i.e., $\delta\mathbf{m} = -\nabla\phi$, evaluated at the starting model $\mathbf{m}_0$ depicted in Figure 12 (b). The results for $K = 10$ and $K = 80$ are included in Figures 12 (c,d). We calculated the error bars from 5 independent realizations. As we increase $K$, the true objective is better approximated reflected in tighter and better centered (compared to the true objective) error bars. These results also show that we can substantially reduce the computational costs while approximating the true objective function accurately.

*WEMVA on the Marmousi model*

To validate our approach to WEMVA based on random probing and full-subsurface offert common-image point gathers (CIPs), we minimize the approximate objective in equation  with a quasi-Newton method using approximate evaluations for the objective (equation 18) and gradients (equation 20). We choose the Marmousi model plotted in Figure 13 (a), because of its complexity and relatively steep reflectors. The model is 3.0 km deep and 9.2 km wide, sampled at 12 m. We acquired synthetic data for this model using a split-spread acquisition geometry resulting in 767 sources and receivers sources sampled at a 12 m interval. The data simulation and inversion are carried out over 201 frequencies, sampled at 0.1 Hz ranging from 5 to 25 Hz and scaled by a Ricker wavelet with a central frequency of 10 Hz.

We use a highly smoothed starting model with small (or no) lateral variations to start

the inversions for different numbers of probing vectors, $K = 10$ and $K = 100$ respectively. To regularize the inversion, we use B-splines sampled at $x = 48\,\mathrm{m}$ and $z = 48\,\mathrm{m}$ in the lateral and vertical directions. Figures 13 (c, d) show the inverted models after 25 L-BFGS iterations. We can clearly see that even 10 probing vectors are good enough to reveal the structural information. Compared to computing the full image gathers (which would need $2 \cdot 767$ PDE solves per evaluation), this reduces the computational cost and memory use by roughly a factor 60.

Encouraged by this result, we conduct a second experiment for a poor starting model (Figure 14 (b)) and for data with fewer low frequencies ($8 - 25\,\mathrm{Hz}$). In this case, we use a slightly higher number of probing vectors ($K = 100$) to reduce the error in approximating the true objective function. Figures 12 (c, d) show that the errors for small $K$ are relatively large when the starting model is poor. This is the case for small $\alpha$'s in Figure 12. To regularize the inversion, we use B-splines sampled at $x = 96\,\mathrm{m}$ and $z = 96\,\mathrm{m}$ in the lateral and vertical directions in order to recover the smooth (low-frequency) component of the true velocity model. We can clearly see in Figure 14 (c) that we build the low-frequency component of the velocity model. Figure 14 (d) shows our velocity estimate overlaid with a contour plot of the true velocity perturbation. We can see that despite missing low frequencies the inverted model captures the shallow complexity of the model reasonably well.

## DISCUSSION

To our knowledge this work represents the first instance of deriving a discrete two-way equivalent of Claerbout's double square-root equation (Claerbout, 1970, 1985a) that enables us to compute full-subsurface offset extended image volumes. Contrary to approaches based

on the one-way wave equation, which are dip-limited and march along depth, our method provides access to extended image volumes via actions of a wave-equation based factorization on certain probing vectors. This factorization enables matrix-vector products with matrices that encode wavefield interactions between arbitrary pairs of points in the subsurface that can not formed explicitly. As a result, we arrive at a formulation that is computationally feasible and that offers new perspectives on the design and implementation of workflows that exploit information embedded in various types of subsurface extended images.

Depending on the choice of the probing vectors, we either obtain local information, tied to individual subsurface points that can serve as quality control for velocity analyses or as input to localized amplitude-versus-offset analysis, or global information that can as we have shown be used to drive automatic velocity analyses. Aside from guiding kinematical inversions through focusing, we expect that our randomized probings of extended image volumes also provide information on the rock properties. We leave this expect and the generalization of our formulation to include elastic waves, which turns our matrix representation into a tensor representation, to a future paper.

## CONCLUSIONS

Extended subsurface image volumes carry information on interactions between pairs of subsurface points encoding essential information on the kinematics—to be used during velocity analysis—and the dynamics, which serve as input to inversions of the rock properties. While conceptually beautiful, full-subsurface offset image volumes have not yet been considered in practice because these objects are too large to be formed explicitly. Through a wave-equation based factorization, we avoid explicit computations by forming matrix-vector products instead that only require two wave-equation solves each, and thereby removing the

customary and expensive loop over shots, found in conventional extended imaging. This approach leads to significant computational gains in certain situations since we are no longer constrained by costs that scale with the number of shots and the number subsurface points and offsets visited during the cross-correlation calculations. Instead, we circumvent these expensive explicit computations by carrying out these correlations implicitly through the wave equation solves. As a result, we end up with a matrix-vector formulation from which different image gathers can be formed and with which amplitude-versus-angle and wave-equation migration-velocity analyses can be performed without requiring prior information on the geologic dip. We showed that these operations can be accomplished at affordable computational costs.

By means of concrete examples, we demonstrate how localized information on focussing and scattering amplitudes can be revealed by forming different extended image volumes in both 2-D and 3-D. Because full-subsurface extended image volumes are quadratic in the number of gridded subsurface parameters, it would be difficult if not impossible to obtain these results by conventional methods. We also verify that our matrix-vector formulation lends itself well for automatic migration-velocity analysis if Gaussian random probing vectors are used. These vectors act as simultaneous sources and allow for significant computational gains in the evaluation of global focusing objectives that are key to migration-velocity analysis. Instead of focussing in a particular offset direction, as in most current approaches, our objective and its gradient force full-subsurface extended image volumes to focus in all offset directions at all subsurface points. It accomplishes this by forcing a commutation relation between the extended image volume and a matrix that expresses the Euclidean distance between points in the subsurface. The examples show that the computational costs can be controlled by probing. Application of this new automatic migration-velocity analysis

technique to a complex synthetic shows encouraging results in particular in regions with steep geological dips.

## ACKNOWLEDGEMENTS

We would like to thank the BG Group for permission to use the synthetic Compass 3D velocity model, Rafael Lago and Curt Da Silva for setting up the 3D Helmholtz wave-equation solver framework, and three anonymous reviewers for helping to improve the manuscript. We also would like to acknowledge the collaboration of the SENAI CIMATEC Supercomputing Center for Industrial Innovation, Bahia, Brazil, and the support of BG Group and the International Inversion Initiative Project. This work was in part financially supported by the NSERC and the Collaborative Research and Development Grant DNOISE II (375142-08). This research was carried out as part of the SINBAD II project with support from the following organizations: BG Group, BGP, Chevron, ConocoPhillips, DownUnder GeoSolutions, Hess, Petrobras, PGS, Woodside, CGG, Sub-Salt Solutions, and WesternGeco.

## REFERENCES


Aki, K., and P. G. Richards, 1980, Quantitative seismology: Freeman and Co. New York.

Avron, H., and S. Toledo, 2011, Randomized algorithms for estimating the trace of an implicit symmetric positive semi-definite matrix: Journal of the Association for Computing Machinery, **58**, P1–P16.

Bai, B., C. Chen, M. Yang, P. Wang, and Y. Huang, 2013, Ghost effect analysis and bootstrap deghosting application on marine streamer data: 75th EAGE, London, United Kingdom, Expended Abstracts.

Baysal, E., D. D. Kosloff, and J. W. Sherwood, 1983, Reverse time migration: Geophysics, **48**, 1514–1524.

Berkhout, A. J., 1993, A unified approach to acoustical reflection imaging. I: The forward model: The Journal of the Acoustical Society of America, **93**, 2005–2016.

Biondi, B., P. Sava, et al., 1999, Wave-equation migration velocity analysis: 69th Ann. Internat. Mtg Soc. of Expl. Geophys, 1723–1726.

Biondi, B., and W. W. Symes, 2004, Angle-domain common-image gathers for migration velocity analysis by wavefield-continuation imaging: Geophysics, **(5), 69**, 1283.

Bourgeois, A., M. Bourget, P. Lailly, M. Poulet, P. Ricarte, and R. Versteeg, 1991, Marmousi, model and data: Presented at the 1990 workshop on Practical Aspects of Seismic Data Inversion, European Association of Exploration Geophysicists, EAGE.

Brandsberg-Dahl, S., M. de Hoop, and B. Ursin, 2003, Focusing in dip and ava compensation on scattering angle/azimuth common image gathers: Geophysics, **(1), 68**, 232–254.

Chauris, H., M. S. Noble, G. Lambaré, and P. Podvin, 2002, Migration velocity analysis from locally coherent events in 2-d laterally heterogeneous media, part i: Theoretical aspects: Geophysics, **67**, 1202–1212.

Claerbout, J., 1985a, Imaging the earth's interior: Blackwell Scientific Publishers.

Claerbout, J. F., 1970, Coarse grid calculations of waves in inhomogeneous media with application to delineation of complicated seismic structure: Geophysics, **35**, 407–418.

———, 1985b, Fundamentals of geophysical data processing: Pennwell Books, Tulsa, OK.

de Bruin, C., C. Wapenaar, and A. Berkhout, 1990, Angle-dependent reflectivity by means of prestack migration: Geophysics, **(9), 55**, 1223.

Doherty, S. M., and J. F. Claerbout, 1974, Velocity analysis based on the wave equation.: Technical Report 1, Stanford Exploration Project.

Duchkov, A. A., and V. Maarten, 2009, Velocity continuation in the downward continuation approach to seismic imaging: Geophysical Journal International, **176**, 909–924.

Friedlander, M. P., and M. Schmidt, 2012, Hybrid Deterministic-Stochastic Methods for Data Fitting: SIAM Journal on Scientific Computing, **34**, A1380–A1405.

Haber, E., M. Chung, and F. Herrmann, 2012, An effective method for parameter estimation with pde constraints with multiple right-hand sides: SIAM Journal on Optimization, **22**, 739–757.

Koefoed, O., 1955, On the effect of poisson's ratios of rock strata on the reflection coefficients of plane waves: Geophysical Prospecting, **3**, 381–387.

Koren, Z., and I. Ravve, 2011, Full-azimuth subsurface angle domain wavefield decomposition and imaging part i: Directional and reflection image gathers: Geophysics, **76**, S1–S13.

Krebs, J., J. Anderson, D. Hinkley, R. Neelamani, S. Lee, A. Baumstein, and M. Lacasse, 2009, Fast full-wavefield seismic inversion using encoded sources: Geophysics, **(6), 74**, P177–P188.

Kuhel, H., and M. Sacchi, 2003, Least-squares wave-equation migration for avp/ava inver-

sion: Geophysics, **(1), 68**, 262–273.

Kühl, H., and M. D. Sacchi, 2003, Least-squares wave-equation migration for avp/ava inversion: Geophysics, **68**, 262–273.

Kumar, R., T. van Leeuwen, and F. J. Herrmann, 2013, Efficient WEMVA using extended images: Presented at the SEG Workshop on Advances in Model Building, Imaging, and FWI; Houston.

Lago, R., A. Petrenko, Z. Fang, and F. J. Herrmann, 2014, Fast solution of time-harmonic wave-equation for full-waveform inversion: Presented at the EAGE Annual Conference Proceedings.

Levin, S. A., 1984, Principle of reverse-time migration: Geophysics, **49**, 581–583.

Lu, S., N. Whitmore, A. Valenciano, and N. Chemingui, 2014, Illumination from 3d imaging of multiples: An analysis in the angle domain: 84th SEG, Denver, USA, Expended Abstracts.

MacKay, S., and R. Abma, 1992, Imaging and velocity analysis with depth-focusing analysis: Geophysics, **(12), 57**, 1608–1622.

Mahmoudian, F., and G. F. Margrave, 2009, A review of angle domain common image gathers: Technical Report, University of Calgary.

Mulder, W., 2014, Subsurface offset behaviour in velocity analysis with extended reflectivity images: Geophysical Prospecting, **62**, 17–33.

Nocedal, J., and S. J. Wright, 2000, Numerical Optimization: Springer.

Prucha, M., B. Biondi, W. Symes, et al., 1999, Angle-domain common image gathers by wave-equation migration: 69th Ann. Internat. Mtg: Soc. of Expl. Geophys, 824–827.

Ravve, I., and Z. Koren, 2011, Full-azimuth subsurface angle domain wavefield decomposition and imaging: Part 2local angle domain: Geophysics, **76**, S51–S64.

Rickett, J., and P. Sava, 2002, Offset and angle domain common imagepoint gathers for shot profile migration: Geophysics, **(3), 67**, 883–889.

Sava, P., and S. Fomel, 2003, Angle-domain common-image gathers by wavefield continuation methods: Geophysics, **(3), 68**, 1065–1074.

Sava, P., and I. Vasconcelos, 2011, Extended imaging conditions for wave-equation migration: Geophysical Prospecting, **59**, 35–55.

Sava, P. C., and B. Biondi, 2004, Wave-equation migration velocity analysis. I. Theory: Geophysical Prospecting, **52**, 593–606.

Sava, P. C., and S. Fomel, 2006, Time-shift imaging condition in seismic migration: Geophysics, **(6), 71**, S209—-S217.

Shen, P., and W. W. Symes, 2008, Automatic velocity analysis via shot profile migration: Geophysics, **73**, VE49–VE59.

Shuey, R., 1985, A simplification of the zoeppritz equations: Geophysics, **(4), 50**, 609–614.

Stolk, C. C., M. V. de Hoop, and W. W. Symes, 2009, Kinematics of shot-geophone migration: Geophysics, **(6), 74**, WCA19—-WCA34.

Stolk, C. C., and W. W. Symes, 2003, Smooth objective functionals for seismic velocity inversion: Inverse Problems, **19**, 73–89.

Symes, W., 2008a, Approximate linearized inversion by optimal scaling of prestack depth migration: Geophysics, **(2), 73**, R23–R35.

———, 2014, Seismic inverse poblems : recent developments in theory and practice: Proceedings of the Inverse Problems from Theory to Applications Conference, IOP Publishing, 2–6.

Symes, W. W., 2008b, Migration velocity analysis and waveform inversion: Geophysical Prospecting, **56**, 765–790.

Symes, W. W., and J. J. Carazzone, 1991, Velocity inversion by differential semblance optimization: Geophysics, **(5), 56**, 654–663.

Symes, W. W., D. Sun, and M. Enriquez, 2011, From modelling to inversion: designing a well-adapted simulator: Geophysical Prospecting, **59**, 814–833.

ten Kroode, A., D.-J. Smit, and A. Verdel, 1994, Linearized inversed scattering in the presence of caustics: SPIE's 1994 International Symposium on Optics, Imaging, and Instrumentation, International Society for Optics and Photonics, 28–42.

van Leeuwen, T., A. Y. Aravkin, and F. J. Herrmann, 2011, Seismic waveform inversion by stochastic optimization: International Journal of Geophysics, **2011**.

van Leeuwen, T., and F. J. Herrmann, 2014, 3D frequency-domain seismic inversion with controlled sloppiness: SIAM Journal on Scientific Computing, **36**, S192–S217. ((SISC)).

van Wijngaarden, A., 1998, Imaging and characterization of angle-dependent seismic reflection data: PhD thesis, Delft University of Technology.

Whitmore, N., et al., 1983, Iterative depth migration by backward time propagation: Presented at the 1983 SEG Annual Meeting, Society of Exploration Geophysicists.

Yang, T., and P. Sava, 2015, Image-domain wavefield tomography with extended common-image-point gathers: Geophysical Prospecting.

[Table 1 about here.]

[Table 2 about here.]

[Table 3 about here.]

[Figure 1 about here.]

[Figure 2 about here.]

[Figure 3 about here.]

[Figure 4 about here.]

[Figure 5 about here.]

[Figure 6 about here.]

[Figure 7 about here.]

[Figure 8 about here.]

[Figure 9 about here.]

[Figure 10 about here.]

[Figure 11 about here.]

[Figure 12 about here.]

[Figure 13 about here.]

[Figure 14 about here.]

## LIST OF FIGURES

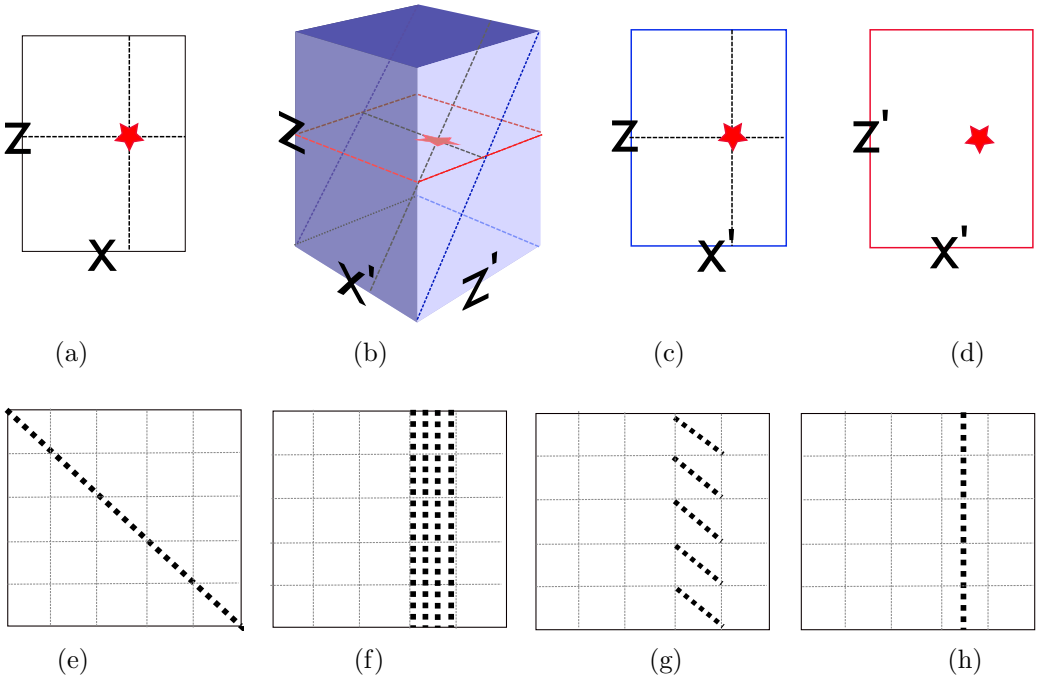


Figure 1: Different slices through the 4-dimensional image volume $e(z, z', x, x')$ around $z = z_k$ and $x = x_k$. (a) Conventional image $e(z, z, x, x)$, (b) Image gather for horizontal and vertical offset $e(z, z', x_k, x')$, (c) Image gather for horizontal offset $e(z, z, x_k, x')$ and (d) Image gather for a single scattering point $e(z_k, z', x_k, x')$. (e-g) shows how these slices are organized in the matrix representation of $e$.

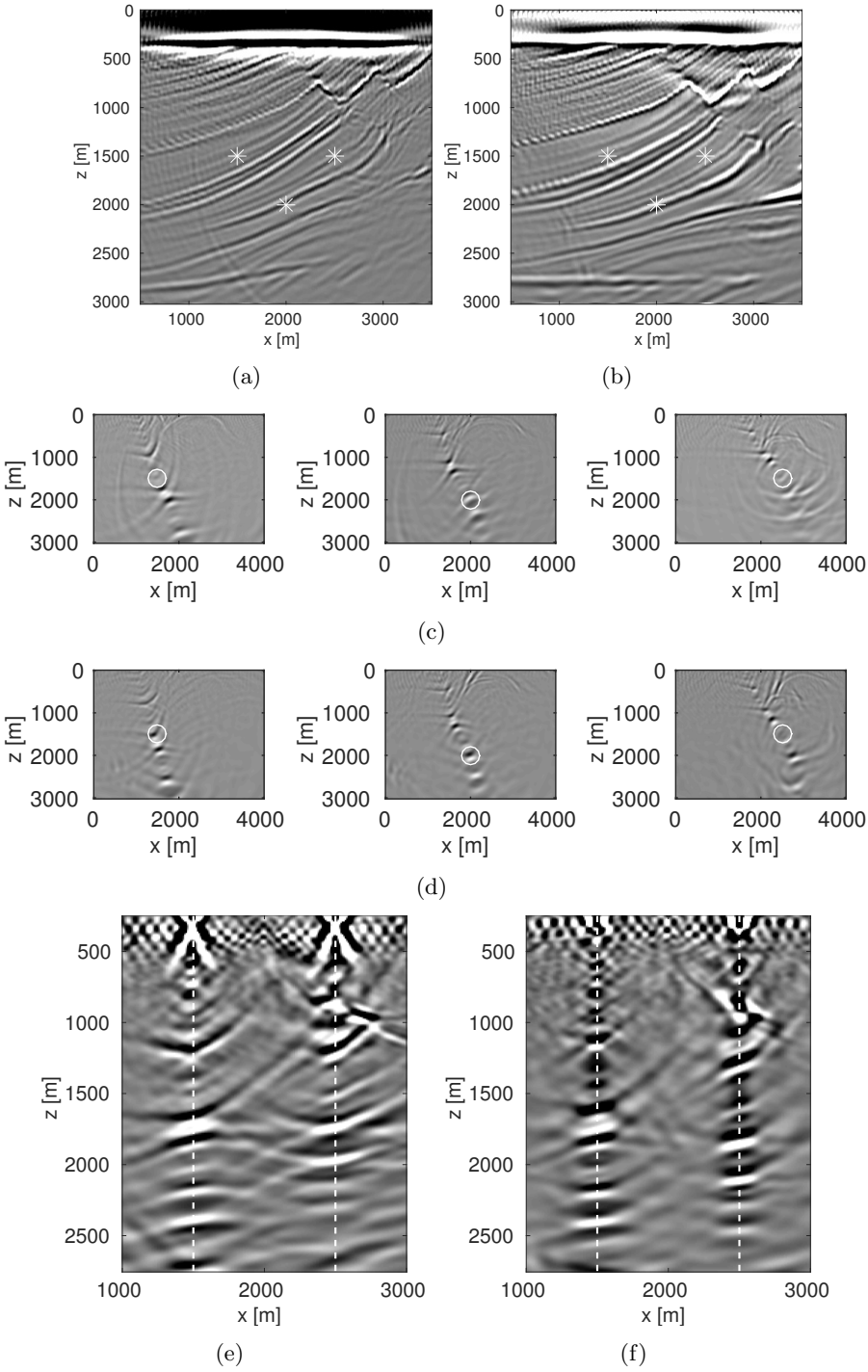


Figure 2: Migrated images for a wrong (a) and the correct (b) background velocity are shown with 3 locations at which we extract CIPs for a wrong (c) and the correct (d) velocity. The CIPs contain many events that do not necessarily focus. However, these events are located along the line normal to the reflectors. Therefore, it seems feasible to generate multiple CIPs simultaneously as long as they are well-separated laterally. A possible application of this is the extraction of CIGs at various lateral positions. CIGs at $x = 1500$ m and $x = 2500$ m for a wrong (e) and the correct (f) velocity indeed show little evidence of crosstalk, allowing us to compute several CIGs at the cost of a single CIG.

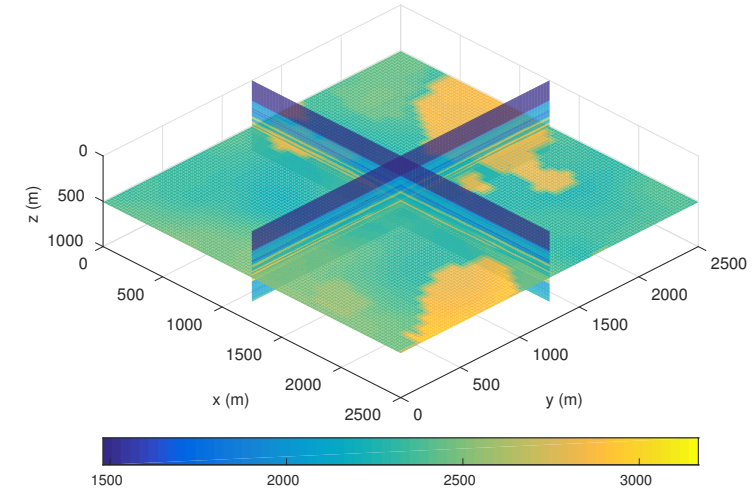


(a)

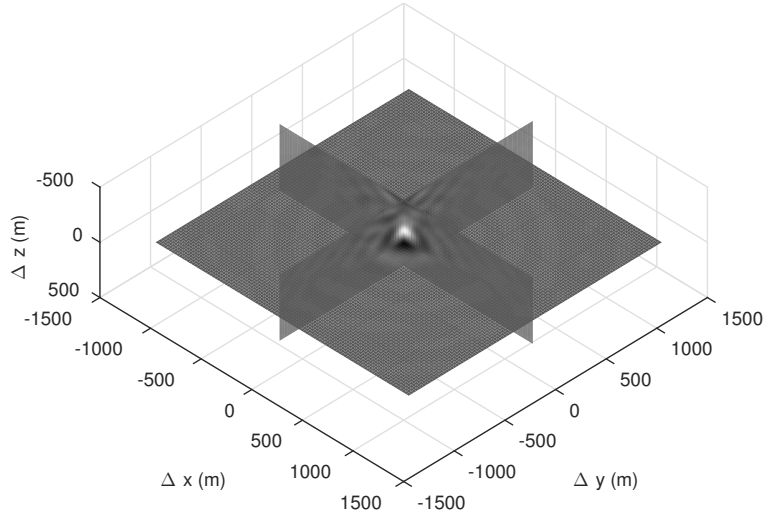


(b)

Figure 3: (a) Compass 3D synthetic velocity model provided to us by BG group. (b) A CIP gather at $(x, y, z) = (1250, 1250, 390)$m. The proposed method (Algorithm 2) is 1500 times faster then the classical method (Algotihm 1) to generate CIP gather.

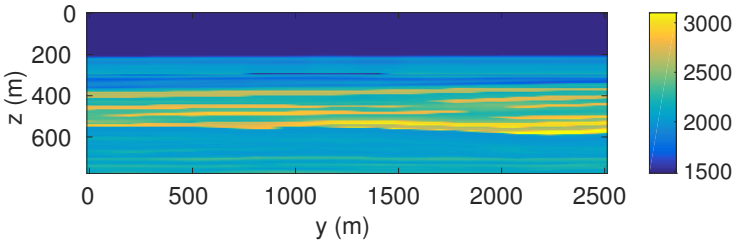


(a)

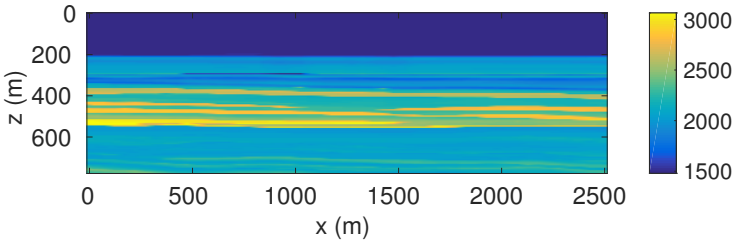


(b)

Figure 4: Cross-section of Compass 3D velocity model (Figure 3 (a)) along (a) x, and (b) y direction.

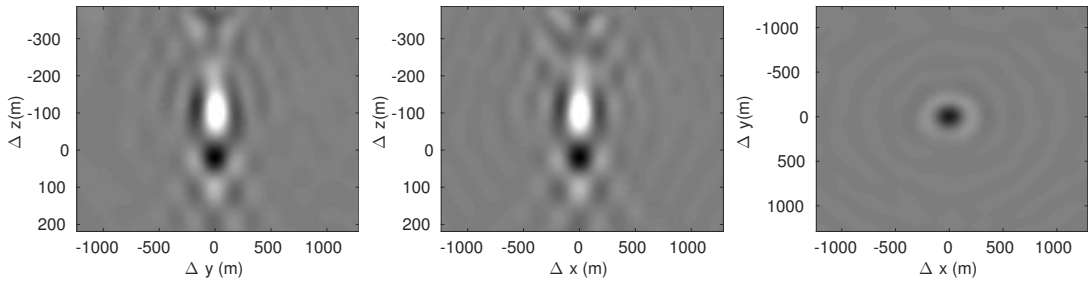


(a) (b) (c)

Figure 5: Slices extracted along the horizontal (a,b) and vertical (c) offset directions from the CIP gather shown in Figure 3 (b).

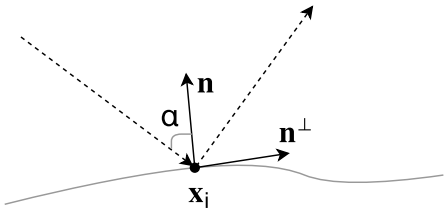


Figure 6: Schematic depiction of the scattering point and related positioning of the reflector.

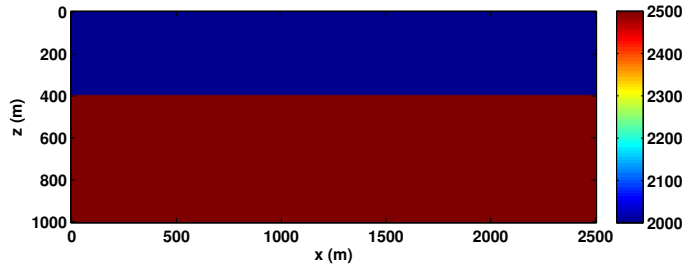


(a)

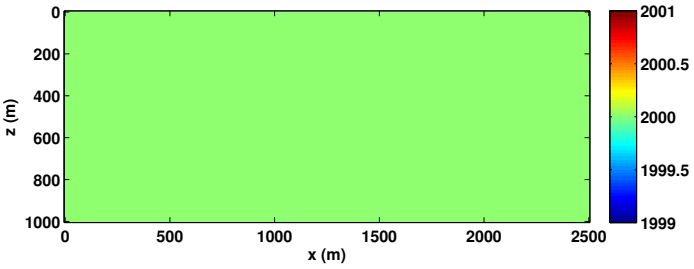


(b)

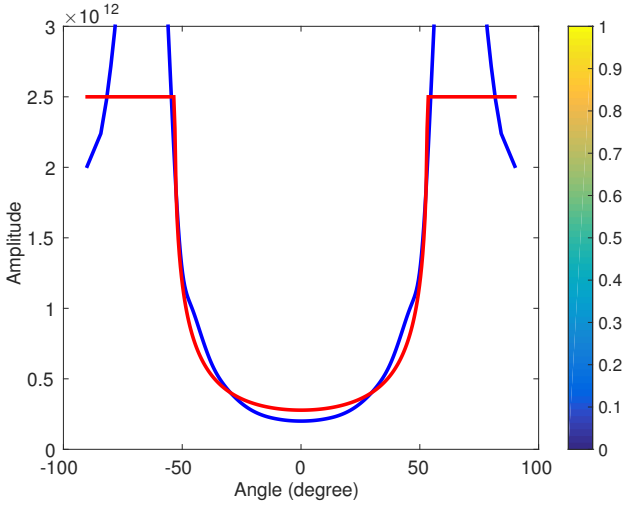


(c)

Figure 7: (a) Horizontal one-layer velocity model and (b) constant density model. CIP location is $x = 1250$ m and $z = 400$ m. (c) Modulus of angle-dependent reflectivity coefficients at CIP. The black lines are included to indicate the effective aperture at depth. The red lines are the theoretical reflectivity coefficients and the blue lines are the wave-equation based reflectivity coefficients.

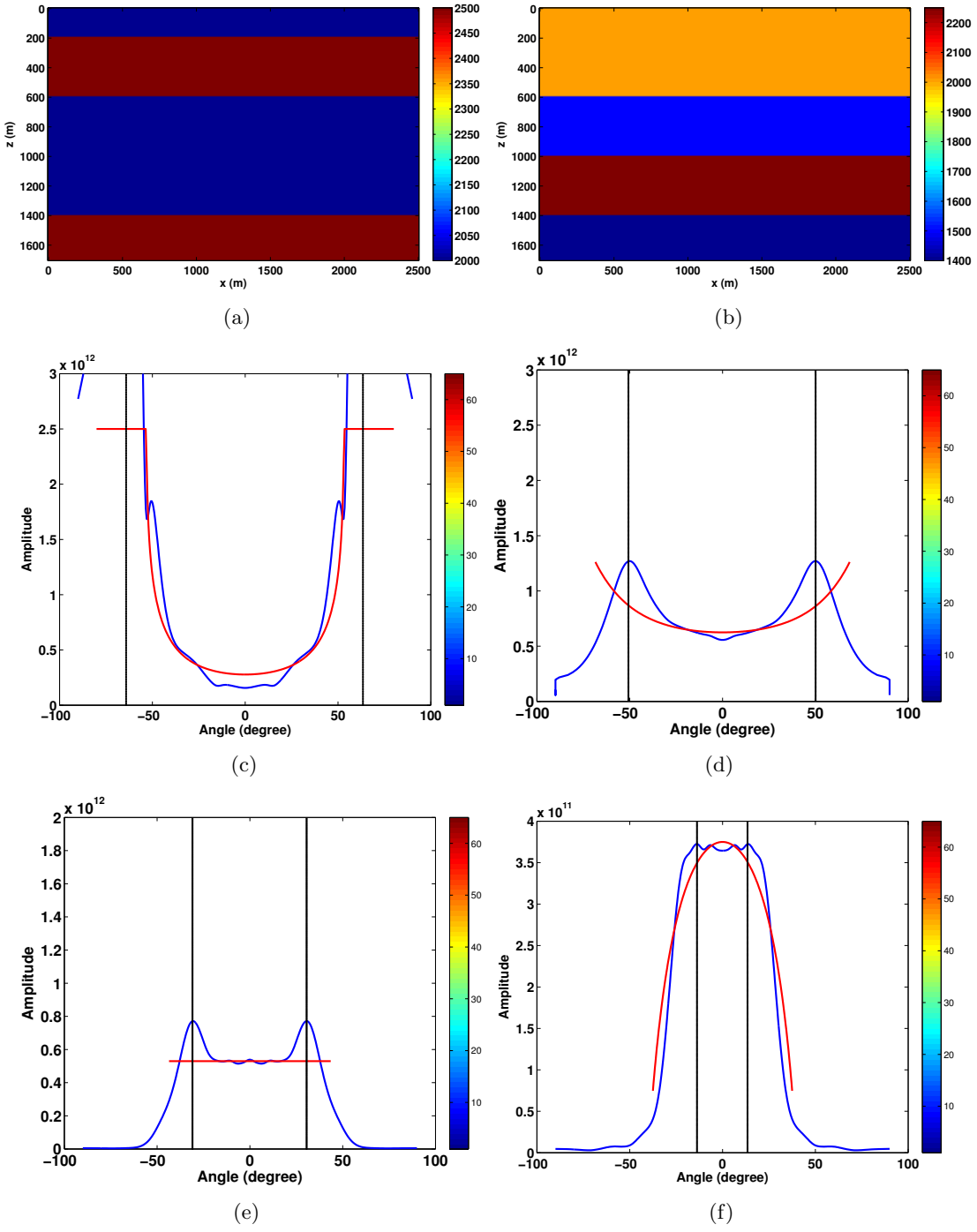


Figure 8: Angle dependent reflectivity coefficients in case of horizontal four-layer (a) velocity and (b) density model at $x = 1250$ m. Modulus of angle-dependent reflectivity coefficients at (c) $z = 200$ m, (d) $z = 600$ m, (e) $z = 1000$ m, (f) $z = 1400$ m.

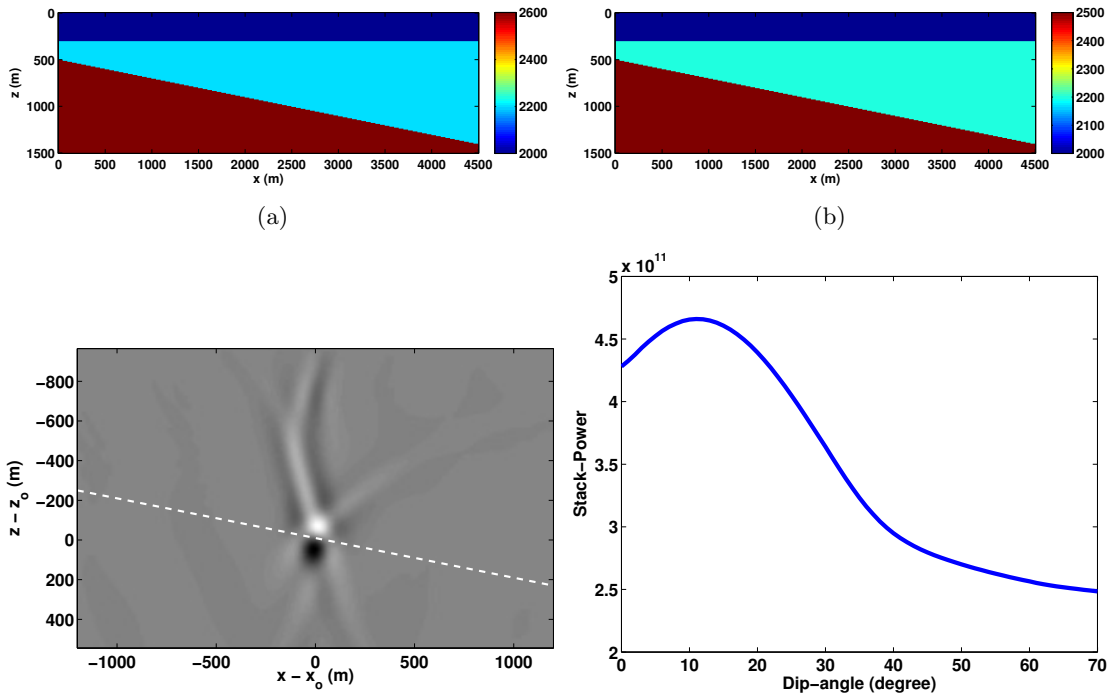


Figure 9: Estimation of local geological dip. (a,b) Two-layer model. (c) CIP gather at $x = 2250$ m and $z = 960$ m overlayed on dipping model. (d) Stack-power versus dip-angle. We can see that the maximum stack-power corresponds to the dip value of 10.8°, which is close to the true dip value of 11°.

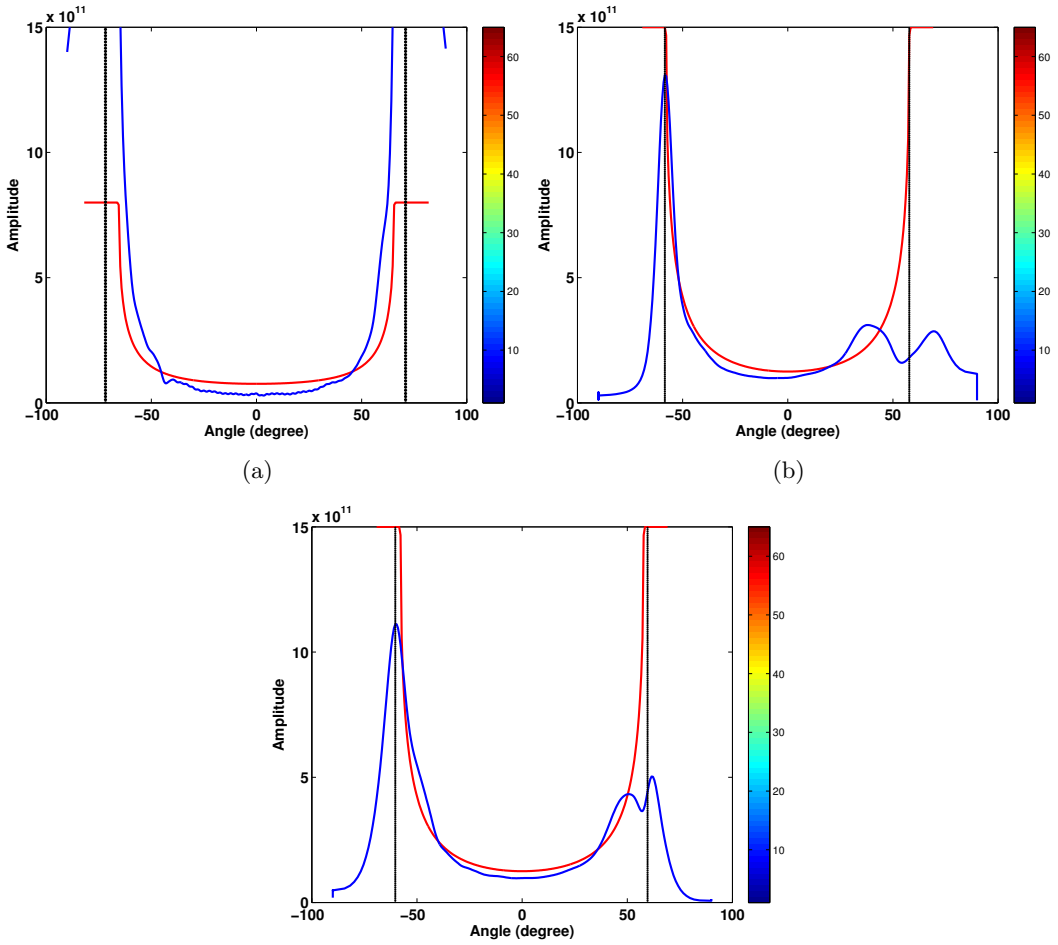


Figure 10: Modulus of angle-dependent reflectivity coefficients in two-layer model at $z = 300$ and 960 m and $x = 2250$ m. (a) Reflectivity coefficients at $z = 300$ m and $x = 2250$ m. Reflectivity coefficients at $z = 900$ m (b) with no dip $\theta = 0°$ and (c) with the dip obtained via the method described above ($\theta = 10.8°$).

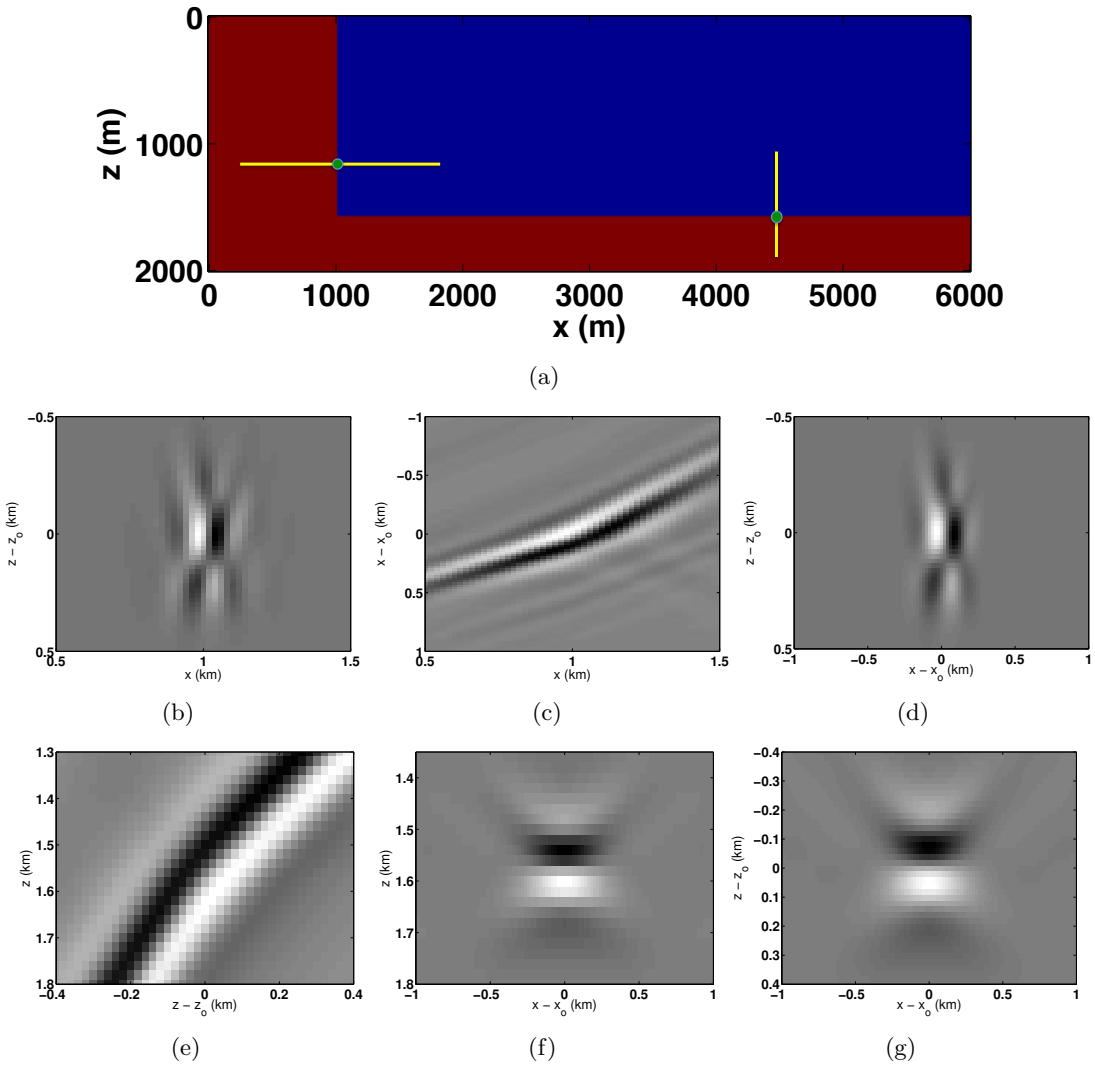


Figure 11: Comparison of working with CIGs versus CIPs. (a) True velocity model. The yellow line indicates the location along which we computed the CIGs and the green dot is the location where we extracted the CIPs. (b,c) CIGs extracted along vertical and horizontal offsets directions in case of vertical reflector. (d) CIPs extracted along vertical ($z = 1.2$ km, $x = 1$ km) reflector. (e,f) CIGs extracted along vertical and horizontal offsets directions in case of horizontal reflector. (g) CIPs extracted along horizontal ($z = 1.5$ km, $x = 4.48$ km) reflector.

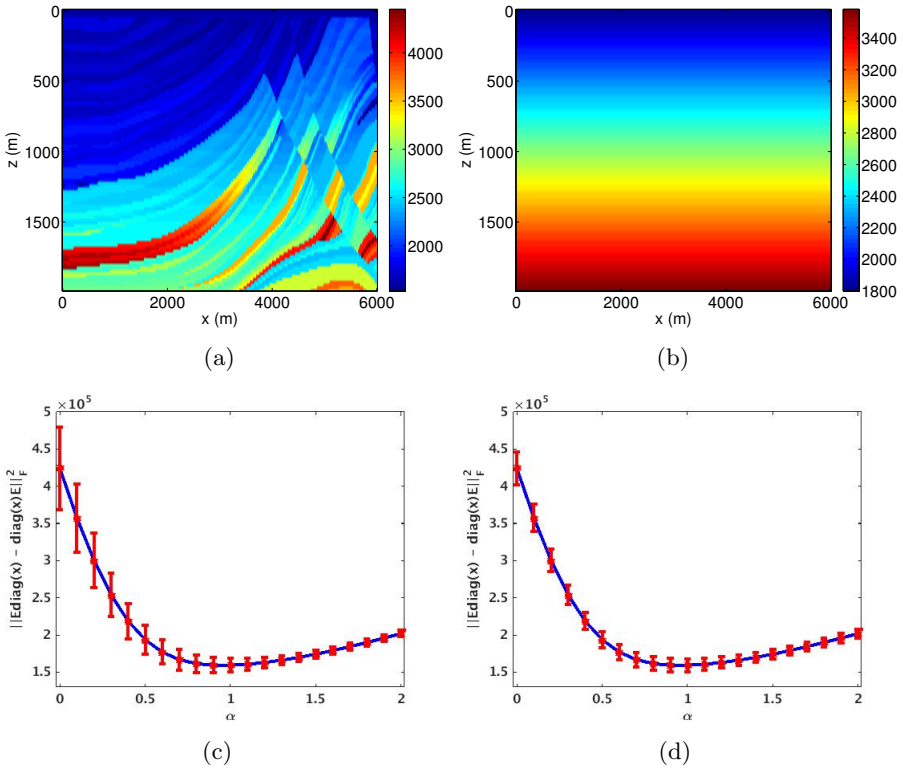


Figure 12: Randomized trace estimation. (a,b) True and initial velocity model. Objective functions for WEMVA based on the Frobenius norm, as a function of velocity perturbation using the complete matrix (blue line) and error bars of approximated objective function evaluated via 5 different random probing with (c) K=10 and (d) K = 80 for the Marmousi model.

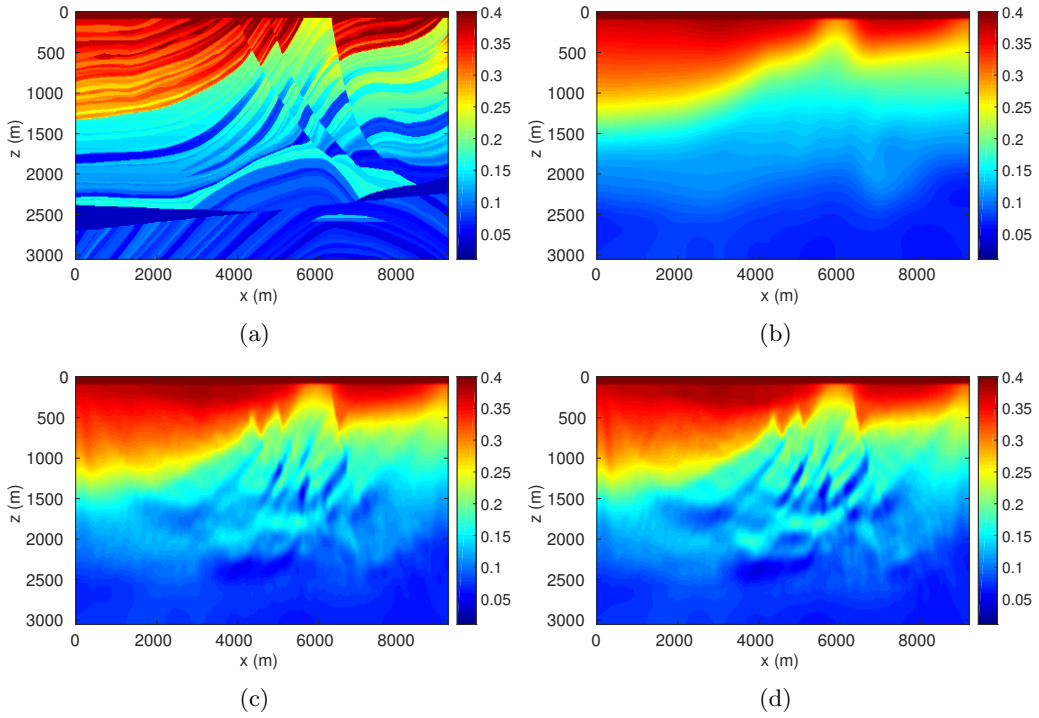


Figure 13: WEMVA on Marmousi model with probing technique for a good starting model. (a,b) True and initial velocity models. Inverted model using (c) $K = 10$ and (b) $K = 100$ respectively. We can clearly see that even 10 probing vectors are good enough to start revealing the structural information.

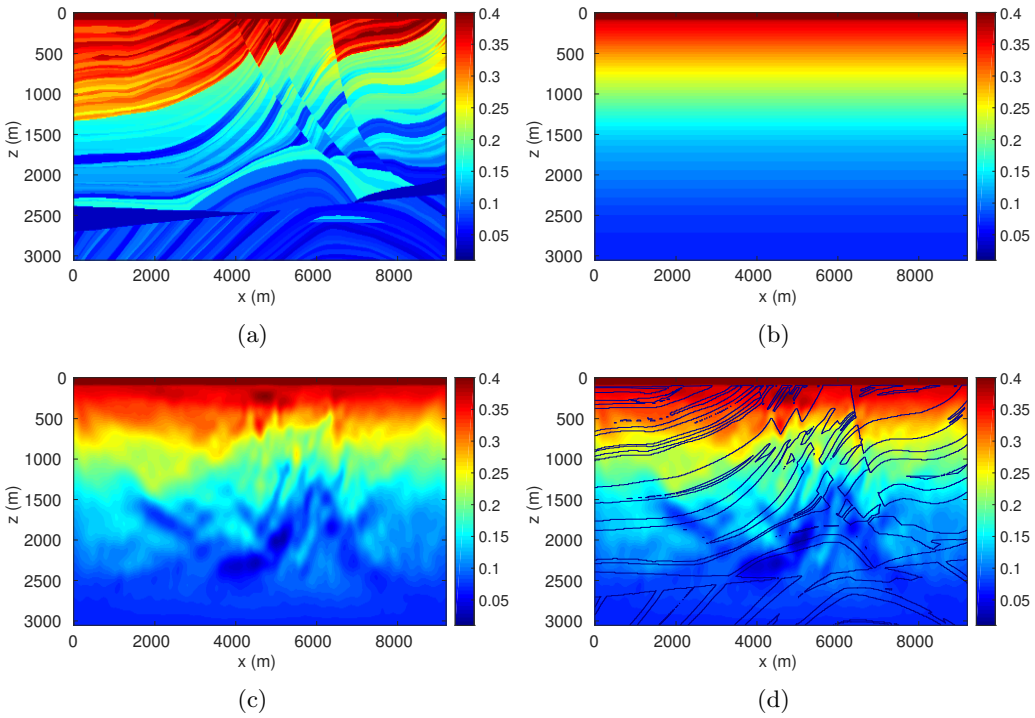


Figure 14: WEMVA on Marmousi model with probing technique for a poor starting velocity model and 8-25 Hz frequency band. (a,b) True and initial velocity models. Inverted model using (c) $K = 100$. (d) Inverted velocity model overlaid with a contour plot of the true model perturbation. We can see that we captures the shallow complexity of the model reasonably well when working with a realistic seismic acquisition and inversion scenario.

## LIST OF TABLES

Table 1: Correspondence between continuous and discrete representations of the image volume. Here, $\omega$ represents frequency, $\mathbf{x}$ represents subsurface positions, and $(i, j)$ represents the subsurface grid points. The colon (:) notation extracts a vector from $e$ at the grid point $i, j$ for all subsurface offsets.

| | Continuous | Discrete |
|---|---|---|
| full image volume | $e(\omega_i, \mathbf{x}, \mathbf{x}')$ | $\mathbf{E}_i$ |
| migrated image | $\int_\Omega \mathrm{d}\omega\ e(\omega, \mathbf{x}, \mathbf{x})$ | $\sum_{i=1}^{N_f} \mathsf{diag}(\mathbf{E}_i)$ |
| CIP | $e(\omega_i, \mathbf{x}_k, \mathbf{x}_{k'})$ | $e_{ikk'}$ |

| | # of PDE solves | flops |
|---|---|---|
| conventional | $2N_s$ | $N_s N_{h_x} N_{h_y} N_{h_z}$ |
| this paper | $2N_x$ | $N_r N_s$ |

Table 2: Computational complexity of the two schemes in terms of the number of sources $N_{\mathrm{s}}$, receivers $N_{\mathrm{r}}$ sample points $N_x$ and desired number of subsurface offsets in each direction $N_{h_{\{x,y,z\}}}$.

| | time (s) | memory (MB) |
|---|---|---|
| conventional | 456 | 152 |
| this paper | 23 | 5.1 |

Table 3: Comparison of the computational time (in sec) and memory (in megabytes) for computing CIP's gather on a central part of Marmousi model. We can see the significant difference in time and memory using the probing techniques compared to the conventional method and we expect this difference to be greatly exacerbated for realistically sized models.